The Astrophysical Journal, 945:143 (15pp), 2023 March 10 https://doi.org/10.3847/1538-4357/acb7da


# A Statistical Study of IRIS Observational Signatures of Nanoflares and Nonthermal Particles

Kyuhyoun Cho[1,2], Paola Testa[3], Bart De Pontieu[2,4,5], and Vanessa Polito[1,2,6]
[1] Bay Area Environmental Research Institute, NASA Research Park, Moffett Field, CA, 94035, USA; cho@baeri.org
[2] Lockheed Martin Solar & Astrophysics Laboratory, 3251 Hanover Street, Palo Alto, CA, 94304, USA
[3] Harvard-Smithsonian Center for Astrophysics, 60 Garden Street, Cambridge, MA, 02193, USA
[4] Rosseland Centre for Solar Physics, University of Oslo, P.O. Box 1029 Blindern, NO-0315 Oslo, Norway
[5] Institute of Theoretical Astrophysics, University of Oslo, P.O. Box 1029 Blindern, NO-0315 Oslo, Norway
[6] Department of Physics, Oregon State University, 301 Weniger Hall, Corvallis, OR, 97331, USA
*Received 2022 November 15; revised 2023 January 17; accepted 2023 January 30; published 2023 March 15*

## Abstract

Nanoflares are regarded as one of the major mechanisms of magnetic energy release and coronal heating in the solar outer atmosphere. We conduct a statistical study on the response of the chromosphere and transition region to nanoflares, as observed by the Interface Region Imaging Spectrograph (IRIS), by using an algorithm for the automatic detection of these events. The initial atmospheric response to these small heating events is observed, with IRIS, as transient brightening at the foot points of coronal loops heated to high temperatures (>4 MK). For four active regions, observed over 143 hr, we detected 1082 footpoint brightenings under the IRIS slit, and for those we extracted physical parameters from the IRIS Mg II and Si IV spectra that are formed in the chromosphere and transition region, respectively. We investigate the distributions of the spectral parameters, and the relationships between the parameters, also comparing them with predictions from RADYN numerical simulations of nanoflare-heated loops. We find that these events, and the presence of nonthermal particles, tend to be more frequent in flare productive active regions, and where the hot 94 Å emission measured by the Atmospheric Imaging Assembly is higher. We find evidence for highly dynamic motions characterized by strong Si IV nonthermal velocities (not dependent on the heliocentric *x*-coordinate, i.e., on the angle between the magnetic field and the line of sight) and asymmetric Mg II spectra. These findings provide tight new constraints on the properties of nanoflares and nonthermal particles in active regions, and their effects on the lower atmosphere.

*Unified Astronomy Thesaurus concepts:* Solar chromosphere (1479); Solar transition region (1532); Solar active regions (1974); Solar physics (1476); Solar coronal heating (1989)

## 1. Introduction

Nanoflares, along with magnetohydrodynamic (MHD) Alfvén waves, are thought to be an important mechanism to explain the heating of the solar corona, which, despite being of fundamental importance in astrophysics, is still not well understood (e.g., Klimchuk 2006; Testa et al. 2015; Testa & Reale 2022). Nanoflares can be produced by magnetic reconnection via braiding of coronal magnetic field lines caused by photospheric motions (Parker 1988). The effect of these small energy releases (thought to be of the order of $10^{24}$–$10^{25}$ erg) is often difficult to observe in the corona because of the high conductivity in the corona efficiently spreading out the energy, and the weak initial emission due to the low emission measure as well as nonequilibrium processes. The lower atmosphere of the coronal loops is more sensitive to the heating release in the initial phases and it provides useful diagnostics of coronal heating (e.g., Testa et al. 2013, 2014).

In the standard model of solar flares, relativistic particles, which are accelerated by magnetic reconnection in the corona, penetrate along the magnetic fields and deposit energy in the chromosphere via collisions (e.g., Holman et al. 2011). Similarly, nanoflares are also expected to generate brightenings in the chromosphere and transition region, and, if indeed they are scaled-down version of larger flares, they might also show the presence of accelerated particles. However, these nonthermal electron beams in nanoflares are likely characterized by shorter durations and smaller energies than in larger flares. Indeed, when nonthermal particles are observed in smaller heating events (nanoflare to microflares), their distributions are typically characterized by smaller low-energy cutoffs and steeper slopes ($E_C \sim 5$–$15$ keV, $\delta \gtrsim 7$; Hannah et al. 2008; Testa et al. 2014; Wright et al. 2017; Glesener et al. 2020; Testa et al. 2020; Cooper et al. 2021) than larger flares, and therefore also penetrating less deep in the low atmosphere.

Recently, small-scale transient brightenings have been reported as the signature of nanoflares in high-resolution and high-cadence observations. Testa et al. (2013) reported that the foot points of hot loops, known as moss, occasionally show high variability in Hi-C 193 Å data. These footpoint brightenings are characterized by timescales of the order of ~15 s, which are much shorter than the known timescales of typically observed moss variability (e.g., De Pontieu et al. 1999; Antiochos et al. 2003). Thus, smaller energies and shorter timescales, compared with larger flares, are required to explain these short-term brightenings. The Interface Region Imaging Spectrograph (IRIS; De Pontieu et al. 2014) provided valuable clues on the heating mechanisms of transient hot loops (Testa et al. 2014, 2020). IRIS provides high temporal and spatial resolution UV spectra formed in the chromosphere and transition region. Comparisons of the observed temporal evolution of spectral properties of IRIS lines with the

prediction of numerical simulations of nanoflare-heated loops indicated that heating by nonthermal electrons is more plausible than conduction to explain some of the observations (Testa et al. 2014, 2020). Polito et al. (2018) and Testa et al. (2020) performed RADYN simulations to show the effect of several physical parameters of nanoflares (e.g., duration, total energy, and low-energy cutoff of nonthermal electron distribution), as well as the initial conditions of the loops, on the observable spectra. They showed that, when nonthermal electrons are present, the energy deposition layer in the lower atmosphere will be determined by the density of the coronal loops and the hardness and total energy of the electron beam. Consequently, the properties of the heating also determine the signs of the Doppler velocities, and the intensities of the chromospheric and transition region lines. Bakke et al. (2022) recently used the same RADYN simulations to investigate additional chromospheric diagnostics of the heating properties based on ground-based spectral observations. These numerical models provide a useful framework to interpret observed spectra.

Recent IRIS observational studies of these footpoint brightenings have analysed a limited number (about a dozen; Testa et al. 2014, 2020) of events, manually selected, precluding any definitive conclusion on the general properties of nanoflares, and the presence and properties of nonthermal particles, in active regions, outside large flares. In order to overcome these limitations we performed statistical studies of the properties of nanoflare events, by using an automated selection procedure to identify a large sample of events, and therefore also reducing some selection biases possibly present in previous studies. For this purpose, we exploit the several EUV images observed by the Atmospheric Imaging Assembly (AIA; Lemen et al. 2012) on board the Solar Dynamics Observatory (SDO; Pesnell et al. 2012) to detect moss locations, and investigate the IRIS spectra obtained at those locations for four different active regions. We apply a modified version of the automated algorithm of Graham et al. (2019) to detect footpoint variability automatically in co-aligned AIA-IRIS data sets of several active regions, and to extract the IRIS spectral line properties (intensity, Doppler shift, and broadening) of Mg II and Si IV for all transient brightenings caught under the IRIS slit. Through an analysis of the statistical distribution of the physical quantities, and of the correlations between different parameters, we determined the general characteristics of nanoflares and their effects on the lower atmosphere. We also compare our finding with previous observational studies and numerical simulation results, and discuss the effect of nanoflares on the lower layer in terms on plasma dynamics and heating mechanism.

## 2. Observation and Analysis

We searched the IRIS database for observations suitable to detect transient loop footpoint brightenings and their chromospheric and transition region emission. We limited the search to sit-and-stare mode, including the Si IV 1402.77 Å and Mg II h&k spectral windows, with a raster scan cadence of less than 15 s to ensure high cadence for the spectral observations. We searched for IRIS data sets including several observations of the same active region over several days, so we can also investigate the dependence of the observed heating properties along the line of sight, and on the active region activity level. Using `ssw_hcr_query.pro` in IDL SolarSoft, we searched the IRIS observing time for every active region from active region number 11800 to 13050 on the solar disk. It is possible that our approach means that data before the assignment of an active region number might not be included. In addition, only IRIS data coincident in time with relevant AIA data without gaps due to missing data or eclipses were selected. Here we present an analysis of IRIS observations for four suitable active regions.

As in Graham et al. (2019), small-scale transient brightening moss regions are identified in AIA data. We used the co-aligned AIA data cubes produced for each IRIS observation, and available on the IRIS search page.[7] After exposure time normalization, we applied the rapid varying moss detection algorithm (Graham et al. 2019) to the co-aligned AIA data. Here we briefly describe the algorithm. We identify the network region with AIA 1700 Å emission above a threshold (>80 digital number (DN)). Then, we select data sets where hot loops are present because we want to investigate the moss variability related to coronal heating events producing hot loops. The Fe XVIII emission in the AIA 94 Å passband traces plasma hotter than ∼4 MK. In particular, to separate the Fe XVIII emission from the other cooler contributions to the 94 Å emission we employed the following simple relation using data from three different AIA channels (Del Zanna 2013):

$$I_{\mathrm{Fe\,XVIII}} = I_{94} - \frac{I_{211}}{120} - \frac{I_{171}}{450}. \quad (1)$$

We chose pixels where the Fe XVIII emission is greater than 5 DN, and the size of the coronal hot loop is larger than 100 pixels, which is an empirical value for the minimum size of a coronal loop. To select bright moss emission, we identify regions with an AIA 193 Å intensity greater than 1250 DN. Even after all these criteria have been applied, it is possible that the selected areas might be associated with other phenomena such as filament eruptions or large flares. To eliminate these possibilities, we used the differential emission measure (DEM) method (Cheung et al. 2015): we excluded areas where the emission measure in two temperature bands $\log T = 5.6$–$5.8$ and $\log T = 6.7$–$7.0$ is greater than $2 \times 10^{26}$ cm$^{-5}$ and $2.5 \times 10^{27}$ cm$^{-5}$, respectively, and their areas are smaller than 15 pixels. We manually confirmed that this method effectively removes flares and filament eruption in most cases. Because we are interested in transient brightening events, we investigated the temporal variation at 171 and 193 Å and selected the local maximum in the light curve. From the first derivative of the light curve, we selected the times when its sign changed from positive to negative, known as zero-crossings (e.g., Testa et al. 2013; Graham et al. 2019).

After identifying the position and time of the moss brightenings in the AIA data, we checked the corresponding IRIS slit positions and observing times. If the IRIS data set includes 1400 Å slit-jaw images (SJIs), we repeated the alignment process of these with the AIA 1600 Å images to increase the accuracy of the IRIS-AIA alignment. We collected every IRIS raster pixel which is corresponding spatially and temporally, within 1″ and 6 s, to the selected AIA moss position and time. We set an additional criterion using the Si IV spectral line. We produce Si IV light curves by deriving the temporal evolution of the Si IV total intensity obtained by

[7] https://iris.lmsal.com/search/

**Table 1**
Information about the Targeted Active Regions

| Active Region Number | Observing Times (hr) | Selected Number of Moss Pixels | Number of Flares[a] (C/M/X) | The Mount Wilson Magnetic Classification[a,b] |
|---|---|---|---|---|
| 12415 | 47.98 | 362 | 36/2/0 | $\beta$ / $\beta\gamma$ |
| 12473 | 43.63 | 439 | 30/5/0 | $\beta$ / $\beta\gamma$ / $\beta\delta$ / $\beta\gamma\delta$ |
| 12524 | 11.09 | 36 | 3/0/0 | $\alpha$ / $\beta$ |
| 12529 | 40.28 | 245 | 30/1/0 | $\alpha$ / $\beta$ / $\beta\gamma$ |
| Total | 142.98 | 1082 | | |

**Notes.**
[a] http://helio.mssl.ucl.ac.uk/helio-vo/solar_activity/arstats-archive.
[b] Hale et al. (1919); Künzel (1965).

integrating over $1402.77 \pm 2$ Å. The light curves are obtained for an interval of $\pm 150$ s from the moss detection instant in each pixel. Then, we investigated if an intensity peak exists within $\pm 30$ s from the moss detection instant, and the intensity peak value is greater than $3\sigma$ of the light curve from the base intensity. We also checked that the intensity peak has a lifetime (FWHM) shorter than 60 s. If the Si IV light curve satisfies these three conditions the event is marked as a moss brightening and included in our sample. Then, using the $\chi^2$ values from the spectral fitting, as described later, we discard the bottom 1%, which effectively eliminates poorly fitted spectra. Finally, we conducted the investigation on the spectral properties at the peak time of the Si IV light curve in each pixel. For the Mg II spectral analysis, we used the peak time of the Mg II k light curve in each pixel obtained by integrating within $\pm 0.65$ Å of its central wavelength. As a result, a total of 1082 pixels were obtained from 747 moss brightening events, and only the peak time properties were taken from each pixel. The information and number of selected pixels for each active region is summarized in Table 1.

We collect the spatial information for the IRIS moss brightenings. The heliocentric coordinates of the pixels provide information about the inclination of the local vertical with respect to the line of sight. Under the reasonable assumption that, on average, the magnetic field in the transition region foot points of hot active region loops is typically vertical, this then provides a constraint on the dependence with respect to the magnetic field direction. The spatially averaged Fe XVIII emission for whole data field of view (FOV) provided with the IRIS data was collected as an auxiliary value for the environment of the event.

We extract the spectral parameters by fitting the IRIS spectra normalized by their exposure time. For the Si IV spectra, we use a single Gaussian function to fit the $1402.77 \pm 2$ Å wavelength range and obtain the three parameters—amplitude, centroid, and width—from which we derive the intensity amplitude, Doppler velocity, and nonthermal velocity, respectively. The nonthermal velocity was acquired by subtracting the thermal broadening and the instrumental broadening as follows:

$$w_{\rm nth} = \sqrt{w_{\rm obs}^2 - w_{\rm th}^2 - w_I^2}, \quad (2)$$

where $w_{\rm nth}$ is the nonthermal velocity, $w_{\rm obs}$ is the $1/e$ width of the Si IV line, which corresponds to $\sqrt{2}$ times the Gaussian width, $w_{\rm th}$ is the thermal velocity, which corresponds to about 6.9 km s$^{-1}$ for the Si IV 1402 Å, and $w_I$ is the instrumental broadening, which is of the order of 3.3 km s$^{-1}$ for the IRIS far-ultraviolet (FUV) spectral band (De Pontieu et al. 2014).

We also calculated the plasma electron density using the diagnostic based on the O IV 1399 Å to 1401 Å line ratio.[8] We obtained the O IV total line intensities by integrating between $1399.77 \pm 0.25$ Å and $1401.16 \pm 0.25$ Å, respectively, and then calculated the line ratio. We exclude samples for which total line intensity is lower than $3\sigma$, where $\sigma$ is defined by following equation:

$$\sigma_{\rm line} = \sqrt{N_{\rm pix}\,\sigma_{\rm bg}^2}, \quad (3)$$

where $\sigma_{\rm line}$ is the $\sigma$ of the total line intensity, $N_{\rm pix}$ is the number of spectral pixels for each O IV line, and $\sigma_{\rm bg}$ is the standard deviation of the background spectra in the wavelength range $1404.25 \pm 0.25$ Å, where no noticeable spectral lines exist (Curdt et al. 2004). We collect the density information in 55% (593/1082) of the pixels. The others have a line ratio outside of the theoretically expected range between 0.17 and 0.42 for density diagnostics, or fail the $3\sigma$ detection criterion. These two groups have a large overlap.

For the Mg II h&k lines, we measured the velocity using two different methods. First, we calculate the centroid of the spectra using the center of gravity method in the range within $\pm 0.65$ Å of their central wavelengths, and convert these values to velocities:

$$v_{\rm center} = \frac{c}{\lambda_0}\frac{\int(\lambda - \lambda_0) I_\lambda\, d\lambda}{\int I_\lambda d\lambda}, \quad (4)$$

where $v_{\rm center}$ is the centroid velocity, $c$ is the speed of light, $\lambda$ is the wavelength, $\lambda_0$ is the central wavelength of the line, and $I_\lambda$ is the observed spectrum. This centroid velocity roughly reflects the average motion within the chromosphere because the formation height of the Mg II h&k lines spans a relatively wide height range. Second, we measure the Mg II h3 and k3[9] Doppler velocities. As in Schmit et al. (2015), we adopted a combination of two symmetric linear functions, and a positive and a negative Gaussian function to fit each line. This function is coded as `iris_mgfit.pro` in IDL SolarSoft. We determined the k3 and h3 positions from the fitted spectral curve through `iris_postfit_get.pro`, which is also included in IDL SolarSoft, then these spectral positions were converted to velocities. If the measured h3 and k3 velocities

[8] https://iris.lmsal.com/itn38/diagnostics.html##density-diagnostics
[9] See Figure 3.2 in https://iris.lmsal.com/itn39/Mg_diagnostics.html##the-mg-ii-h-k-lines.

well represent the dynamics at the $\tau = 1$ layer, like in numerical simulations of the quiet Sun (Leenaarts et al. 2013), they can provide valuable information about the upper chromospheric dynamics. However, the findings by Leenaarts et al. (2013) might not necessarily apply to the very dynamic active region plasma we are investigating here. Futhermore, in some cases the observed Mg II spectra are either single peaked, or have multiple (>2) peaks, so it is not always easy to determine the h3 and k3 positions. In fact, about 19% of the Mg II k lines (206/1082) and Mg II h lines (203/1082) show single peak profiles, and about 16% of the cases (107/1082) show single peak profiles in both spectral lines. The single peaks are often accompanied by highly shifted tiny k3 or h3 self-absorption features. To avoid misidentifications, we excluded those from the Mg II parameters analysis. On the contrary, the centroid method is free from this problem, so we mainly use centroid velocities to investigate the chromospheric dynamics, and the h3 and k3 velocities are used as supplementary parameters. As we will discuss later, another advantage of the centroid analysis is that comparisons with the RADYN simulations (Polito et al. 2018; Testa et al. 2020) are more straighforward as the synthetic Mg II profiles are often quite complex, rendering determination of the k3 and h3 Doppler shifts difficult.

Another important feature is the Mg II triplet line at 2798.823 Å. Numerical simulations in Testa et al. (2020) showed that this line is expected to be observed as an emission line when nonthermal electron of sufficient energy ($\gtrsim$10 keV) are present, as they will deposit energy and locally heat the lower chromospheric layer. In general, the Mg II triplet spectrum exhibits a complicate shape, which is like a miniature of the Mg II h&k line: it has dips at both wings and self absorption at the core similar to Mg II h1&k1 or h3&k3, so it is not easy to determine whether it is an emission line or not. To quantify its behavior, we calculated the equivalent width of the Mg II triplet line by integrating yjr spectrum over the $2798.823 \pm 0.2$ Å interval:

$$\mathrm{EW} = \int \frac{I_\lambda - I_c}{I_c}\, d\lambda, \tag{5}$$

where EW is the equivalent width and $I_c$ is the continuum determined by quadrature fitting within the 2797.5–2802.5 Å range. We defined the Mg II triplet to be in emission if its equivalent width is a positive value.

For the comparison with numerical simulations, we adopted the models from Polito et al. (2018) and Testa et al. (2020), which are produced by using the RADYN code (Carlsson & Stein 1992, 1995, 1997a; Allred et al. 2015). That is a one-dimensional hydrodynamic code including nonlocal thermodynamic equilibrium radiative transfer. We obtain the optically thin Si IV synthetic spectra as described in Testa et al. (2014), Polito et al. (2018), and Testa et al. (2020). The Mg II spectra are calculated by using the RH 1.5D radiative transfer code (Uitenbroek 2001; Pereira & Uitenbroek 2015) based on the atmospheric model from the RADYN simulations. Detailed information of the simulation models is summarized in Table 2. All models considered here assume the same initial atmosphere characterized by a ~1 MK loop top temperature, a coronal density of $\sim 5 \times 10^8$ cm$^{-3}$, and a loop length of 15 Mm (see Polito et al. 2018 and Testa et al. 2020 for more details). We analysed the synthetic IRIS Mg II and Si IV spectral profiles at the peak time of their light curves using the same procedure applied to the observed spectra. This allowed us to derive the spectral parameters of the synthetic spectra that can be directly compared with the ones derived from the observed spectra. We note that the different models are characterized by different peak times for the transition region and chromospheric emission.

## 3. Results

Figure 1 shows SDO/AIA observations of the four selected target active regions, and in particular, we show images of the photospheric intensity, line-of-sight magnetic field maps, and 94 Å (in active region cores typically dominated by Fe XVIII emission; Testa & Reale 2012; Cheung et al. 2015) and 193 Å images (where active region moss is bright). Even though the active regions evolved as they crossed the solar disk during their lifetime, their characteristics are reflected in these images. For example, in the case of active region 12524, it shows a relatively simple configuration of magnetic polarities, which is well reflected in its Mount Wilson magnetic classification in Table 1. It shows dimmed 94 Å intensity compared to the other active regions. Throughout the observed period this active region was less active than the other active regions. Here we are interested in identifying and characterizing small heating events and exclude general flares, and we filter them out using the DEM analysis, as described in the previous section. The number of observed flare events in each active region is summarized in Table 1. We found more small-scale transient brightening pixels in active regions where flaring activity is strong and the magnetic field configuration is complex. It is a well known fact that the flare activity of active regions is strongly correlated with their Mount Wilson magnetic classification (Toriumi & Wang 2019, and reference therein). Although the probability of observing brightening pixels is affected by the slit location and observing time, it appears that the small-scale transient brightenings have a relation to the magnetic field configuration as well.

### 3.1. Distributions of the Parameters

The overall distributions of the obtained parameters are shown in Figure 2. The first three parameters (heliocentric $x$-coordinate, Fe XVIII intensity, and the transition region density) in Figures 2(a)–(c) provide us with background information, and in particular the Fe XVIII emission tracks the hot ($\gtrsim$4 MK) emission in the active region, and therefore, to some extent, the coronal activity level. The locations of the brightenings show that they are widely distributed from heliographic east to west. The Fe XVIII intensity and transition region density have somewhat wide ranges of values, and depend on the activity level of the active region at that moment. Active region 12524 shows relatively low Fe XVIII intensity and density, while active regions 12415 and 12473 show higher values, and this tendency is well matched with their flare productivity in Table 1. The values for the duration of the events, according to its definition (see Section 2), are almost uniformly distributed from 0 to 60 s (Figure 2(d)).

In the histograms of the values of the total intensity and amplitude of the Si IV line (Figures 2(e), (f)), it can be seen that the algorithm preferentially found more pixels with smaller values of those parameters. For comparison, the events studied by Testa et al. (2020) show similar or slightly larger ($\gtrsim$40 DN

**Table 2**
Parameters of the RADYN Simulations of Nanoflare-heated Loops

| Model[a] | Total Energy ($10^{24}$ erg) | Flux ($10^9$ erg s$^{-1}$ cm$^{-2}$) | Cutoff Energy (keV) | Spectral Index | Duration (s) |
|---|---|---|---|---|---|
| C1 | 6 | N/A | N/A | N/A | 10 |
| C1+ | 10 | N/A | N/A | N/A | 10 |
| E1 | 6 | 1.2 | 5 | 7 | 10 |
| E1+ | 10 | 2.0 | 5 | 7 | 10 |
| E2 | 6 | 1.2 | 10 | 7 | 10 |
| E2+ | 10 | 2.0 | 10 | 7 | 10 |
| E3 | 6 | 1.2 | 15 | 7 | 10 |
| E3+ | 10 | 2.0 | 15 | 7 | 10 |
| E4 | 6 | 0.4 | 10 | 7 | 30 |
| E5 | 18 | 1.2 | 15 | 7 | 30 |
| E6 | 6 | 0.6 | 10 | 7 | 20+60[b] |
| H1 | 6 | 0.6 | 10 | 7 | 10 |
| H2 | 18 | 0.6 | 10 | 7 | 30 |

**Notes.**
[a] C and E indicate heating by thermal conduction and heating by accelerated electrons, respectively. H indicates hybrid models, which include heating by both local coronal heating and thermal conduction, and accelerated electrons. + indicates a higher total energy ($10^{25}$ erg) model. The model labels follow the naming convention used in Testa et al. (2020).
[b] Intermittent heating: 20 s heating, 60 s pause, and 20 s heating again.

pix$_x^{-1}$ pix$_\lambda^{-1}$ s$^{-1}$) Si IV amplitudes, possibly indicating a bias in their sample toward relatively stronger events because they manually selected the brightening events. The flare productive active regions exhibit higher Si IV total intensities and amplitudes for their brightenings. The observed ranges for these two parameters are well reproduced by the simulations. Among the simulation models, the thermal conduction (C, C+) and high cutoff energy cases (E3, E5) predict lower Si IV intensities. This is not the case for models with an intermediate (10 keV) energy cutoff. For the former two cases, in terms of the thermal conduction and high cutoff energy, the energy is not directly deposited close to the transition region; for the conduction cases, energy will be deposited higher than the transition region, whereas for the higher cutoff energy cases, the energy deposition mostly occurs too deep in the lower atmosphere to significantly affect the Si IV, because the hardness of the electron beam enables the accelerated electrons to reach much deeper regions (Testa et al. 2014; Polito et al. 2018).

The nonthermal velocities of the Si IV emission line have a median $1/e$ width value of about 32 km s$^{-1}$ with a broad distribution up to ~150 km s$^{-1}$ (Figure 2(g)). About half of the pixels (53%) have Si IV nonthermal velocity values between 20 and 40 km s$^{-1}$. This result is higher than the previous reported mean value of the nonthermal velocity within a whole active region (15–20 km s$^{-1}$; De Pontieu et al. 2015). Here, however, we selected active locations undergoing brightening, likely explaining the larger nonthermal velocities. We investigated Si IV spectral profiles with extremely high nonthermal velocities by visual inspection and found that the Si IV line often consists of two or multiple components in those cases. The nonthermal broadening is also higher than we find in the synthetic spectra from the simulations. All of the simulation results show velocities less than 25 km s$^{-1}$, and the synthetic Si IV profiles rarely show multiple emission components. We also found that the active regions with strong flaring activities show higher nonthermal velocities, similarly to the findings discussed above, in terms of the Si IV total intensity and amplitude. Testa et al. (2020) show a histogram of the increase in Si IV nonthermal velocity with respect to its background value outside of heating events (their Figure 6), and their values are between 0 and ~40 km s$^{-1}$, which, considering a background value of the order of 15–20 km s$^{-1}$ (e.g., De Pontieu et al. 2015), would correspond to a range of ~15–60 km s$^{-1}$, which matches well with the bulk of our observations.

In Figures 2(h)–(j), the Si IV mean Doppler velocity shows a slightly downward motion (redshift of ≃4 km s$^{-1}$), and the mean values of the Mg II k and h centroid Doppler velocities are close to 0 km s$^{-1}$. About 62% (672/1082), 61% (657/1082), and 51% (553/1082) of the pixels show a downward motion in the Si IV, Mg II k and h lines, respectively. They show almost symmetric distributions with respect to their mean values, and the standard deviation for Si IV is about 4.5 times larger than those for the Mg II lines, which is reasonable considering the density stratification of the solar atmosphere. These distributions are quite similar for different active regions. The Si IV Doppler velocities from the synthetic spectra show a similar range to what is derived from the observations. Only cases of heating by thermal conduction and with a low cutoff energy show downward motion of the Si IV line. This is consistent with the different energy deposition height for different heating mechanisms and heating properties, and analogous to the Mg II centroid velocity up to −10 km s$^{-1}$. For the Mg II centroids, most models are located near zero velocity except the abovementioned two cases (conduction and 5 keV) and the hybrid models, which have larger downward motions.

The equivalent width values of the Mg II triplet range from −0.1 to 0.3 Å with a median value of −0.02 Å and a standard deviation of 0.16 Å (Figure 2(k)). About 36% (394/1082) of the pixels show positive equivalent width values, which correspond to the Mg II triplet emission. This finding is also consistent with the results from the small sample of events analysed by Testa et al. (2020), where they found Mg II triplet emission in some locations for 4 out of 10 events. Similar to the Si IV parameters, active region 12473 shows slightly higher equivalent width values than the others. Their distribution is roughly similar to the range of the simulation results. The simulation results tend to have higher equivalent width values

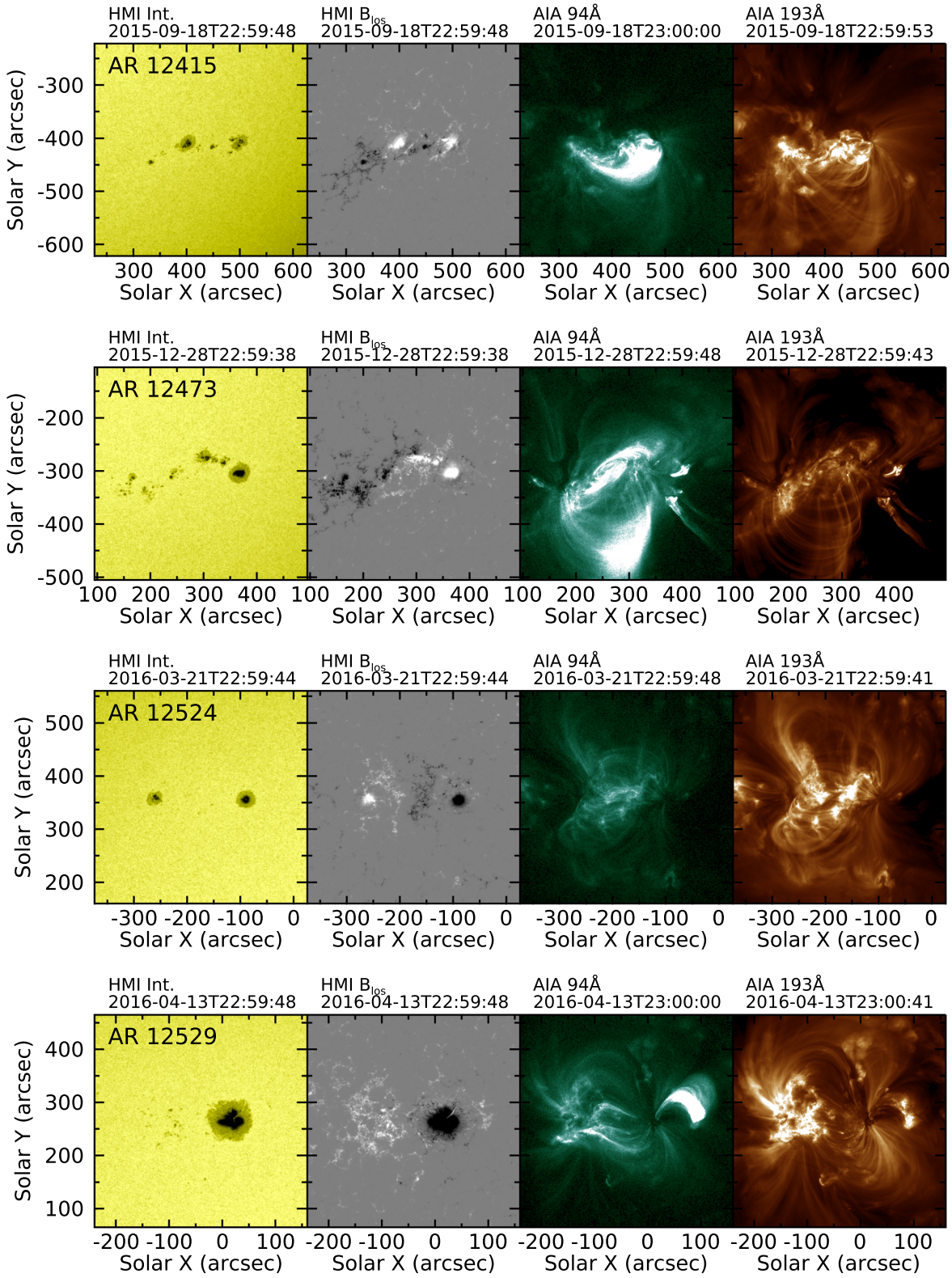


**Figure 1.** Targeted active region images. Each column shows the SDO/Helioseismic and Magnetic Imager continuum intensity, line-of-sight magnetogram, and AIA 94 Å and 193 Å data. Each row indicates a different active region.

with a higher cutoff energy and higher flux. The heating by thermal conduction with a higher total energy (model C1+) shows the smallest equivalent width (EW = −0.10), and the heating by accelerated electron with a cutoff energy of 15 keV and a higher total energy of $10^{26}$ erg (model E3+) shows the largest equivalent width (EW = 0.46). Most of observational results are consistent with the predictions of the simulations with a lower cutoff energy (E1 and E1+), or intermediate cutoff energy (10 keV) and a low-energy flux and total energy (E4, E6, and H1).

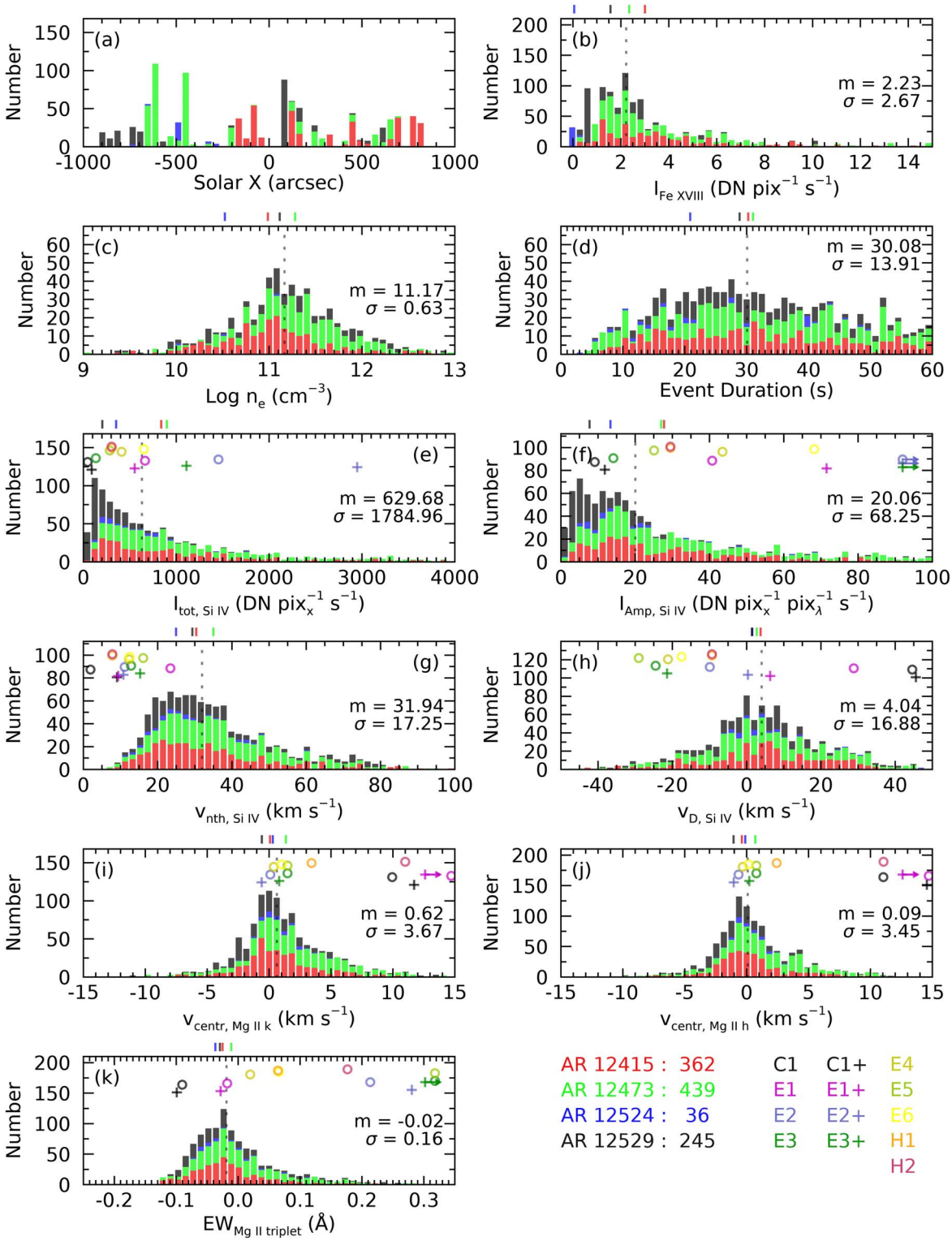


**Figure 2.** Histograms, for the selected footpoint brightenings observed with IRIS, of the following parameters: (a) heliocentric *x*-coordinate, (b) mean Fe XVIII intensity for the whole IRIS SJI FOV, (c) electron density from the O IV ratio, (d) event duration, (e) total intensity of the Si IV 1402 Å line, (f) Gaussian amplitude of the Si IV spectrum, (g) Si IV nonthermal velocity, (h) Si IV Doppler velocity, (i) Mg II k centroid velocity, (j) Mg II h centroid velocity, and (k) equivalent width of the Mg II triplet. A negative Doppler velocity represents blueshift (upward) motion. Each color in the histograms indicates a different active region. The median and standard deviation values are written in the right corner of each panel. The vertical dashed lines indicate the median value of each parameter. The small colored vertical bars above each panel indicate the median value of the corresponding active region. The circle and cross symbols in the histogram of the Si IV and Mg II spectral properties represent the values from simulations with arbitrary *y*-offsets, and the colors correspond to the simulation names shown in the bottom right corner. The cross symbols (+) indicate the results from the simulation model with higher total energy. The right arrow represents values from the simulations that are out of the histogram range. The parameters of the simulations are summarized in Table 2.

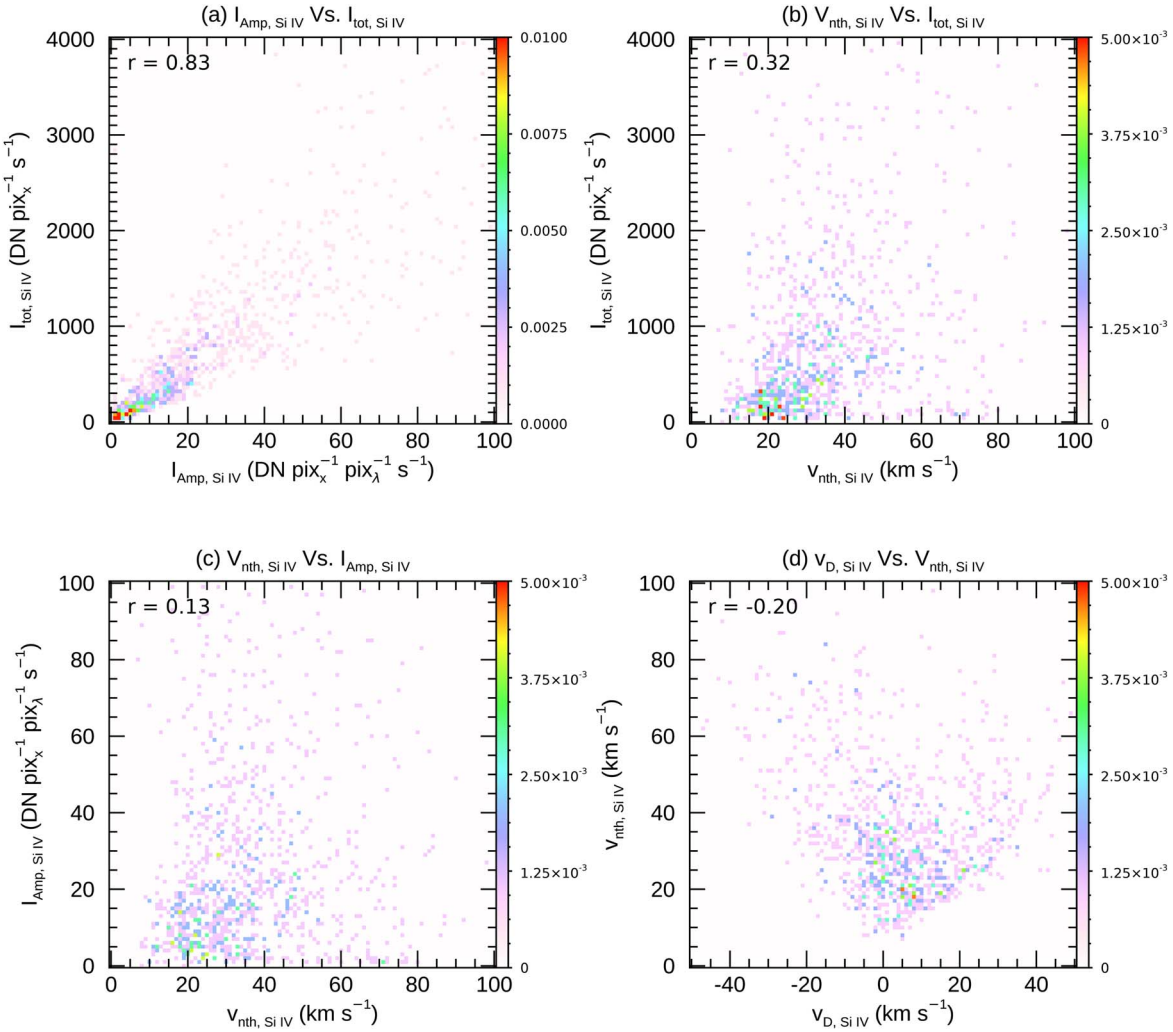


**Figure 3.** Joint probability density functions between the different Si IV parameters: (a) amplitude and total intensity, (b) nonthermal velocity and total intensity, (c) nonthermal velocity and amplitude, and (d) Doppler velocity and nonthermal velocity. The colors indicate the probability density, which is calculated by dividing the number of data points within each bin by the total number of data points. The Pearson correlation coefficient is shown in top left corner of each panel.

### *3.2. Relations Between the Parameters*

We analysed the relations between all parameters (see Figure A1 in the Appendix). Several relations do not show a strong correlation. Especially, the electron density and the event duration do not exhibit strong correlations with the other parameters. However, we found several meaningful relations, and will describe them here below.

#### *3.2.1. Parameters from the Si IV Spectra*

We obtained the total intensity of Si IV through integration of the spectrum (see Section 2 for details). If we ignore the fitting error, the total intensity of the Si IV emission line is approximated by the area of the fitted Gaussian function, and it should be proportional to the Gaussian amplitude and width. In fact, in Figure 3(a), the relation between the total intensity and amplitude of the Si IV line accordingly shows a very strong linear relation with a Pearson correlation coefficient of 0.83, as expected if the observed Si IV line profiles are well fitted with a Gaussian function. Similarly, we found some correlation between the total intensity of the Si IV line and nonthermal velocity (Figure 3(b)), as a proxy of the Gaussian width, but the correlation is only moderate and its correlation coefficient is 0.32, since the line width is basically the combination of thermal, nonthermal, and instrumental width. So the total intensity of Si IV line is more dependent on its amplitude than nonthermal velocity. Testa et al. (2016) find a similar moderate correlation between nonthermal width and line intensity for Fe XII in active region moss.

We also found that the nonthermal velocity is not significantly correlated with the amplitude of the Si IV line (Figure 3(c)). This is in contrast with findings of a previous study of Si IV line properties in a whole active region: De Pontieu et al. (2015) found a correlation between the logarithm of the Si IV intensity amplitude and nonthermal velocity on large scales. A possible reason for the discrepancy might be the presence of multiple emission components in several Si IV spectra. If an emission line has multiple components, its amplitude would relatively decrease while the nonthermal velocity would increase, compared with the corresponding Gaussian with the same total intensity. So, two possibilities can coexist for the low-amplitude spectrum cases: a simple weak event with a small nonthermal velocity, or multiple emission components with large nonthermal velocities. This may be responsible for the observed weak

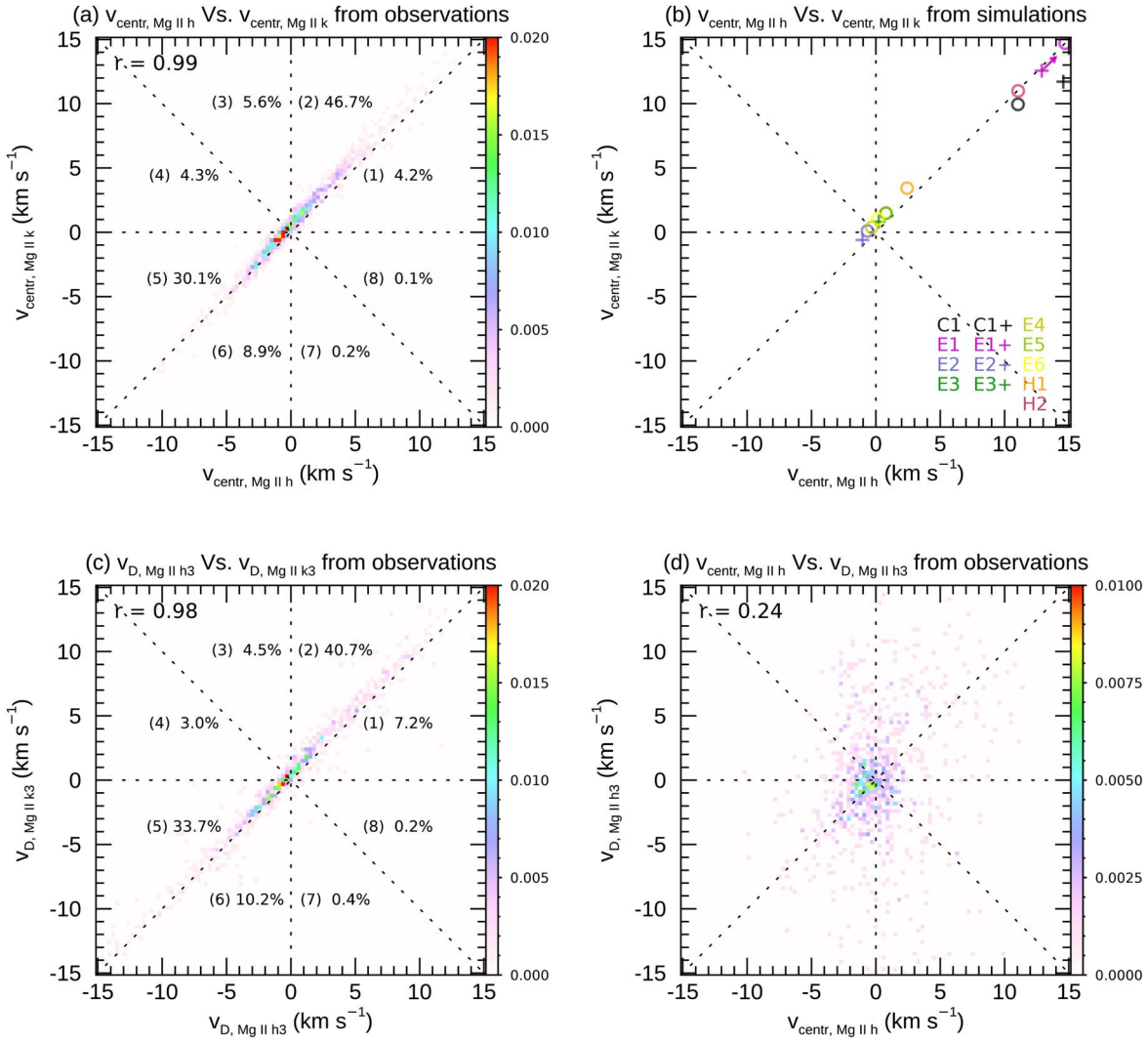


**Figure 4.** (a) Joint probability density functions of the Mg II h & k centroid velocities from the observations. We divided the parameter space into eight areas from (1) to (8) and calculated the percentage of the pixels located in each region. A negative velocity represents a blueshift and upward velocity. (b) Scatterplot of Mg II h & k centroid velocities from the simulations. The names of simulation models corresponding to each color and symbol are presented at the bottom right corner, as in Figure 2. (c) Same as (a), but using the Mg II h3 and k3 Doppler velocities. (d) Joint probability density functions between the Mg II h centroid velocity and Mg II h3 Doppler velocity. The format is the same as in Figure 3.

linear correlation between nonthermal velocity and Si IV amplitude. Another possibility is that these brightenings have a different behavior from the typical active region locations. It is likely that in these regions, which are undergoing heating, the atmospheric structure differs from that of the average active region. After all, we focus on moss brightenings for which it might be more likely to have multiple emission components (some examples were also observed in Testa et al. 2020).

One interesting result is that the joint probability density function between the Si IV Doppler velocity and nonthermal velocity shows an inverted triangle shape distribution (Figure 3(d)). If the nonthermal velocity is close to zero, the Doppler velocity is also close to zero. For higher nonthermal velocity cases, it is possible to have various Doppler velocity values. This implies that some of the nonzero Doppler velocities are related to high nonthermal velocities, i.e., multiple emission components. If so, there is a possibility that the Doppler velocities of moving material may be underestimated.

### 3.2.2. Mg II Doppler Velocities

In Figure 4(a), we found that the centroid Doppler velocities of the Mg II h&k lines show extremely strong correlation ($r = 0.99$), as expected considering that their formation heights are very close to each other and overlapping, so it is very likely that dynamic events affect both lines similarly. Additionally, those two Mg II line velocities have a good correlation with the Si IV Doppler velocity ($r = 0.64$, see Appendix A1). This suggests that the heating occurring in the moss brightenings we analyse here often affects similarly the chromosphere and transition region. Leenaarts et al. (2013) estimated the formation heights of Mg II h3 and k3, and the Mg II line peaks, using three-dimentional radiative MHD simulations of the quiet Sun. They found that the formation height of these spectral features is generally a little bit higher (about 20–50 km) for the k3 line than for the h3 line. This seems also compatible with the relative standard deviation we derive for their Doppler velocities in Figures 2(i) and (j). We therefore can conjecture that the k centroid, and k3 Doppler shift, probe

slightly higher atmospheric layers compared with the corresponding properties of the h line.

Figure 4(a) shows the relation between the Mg II h and k Doppler velocities measured by their centroids. It is clear that both velocities have the same sign in most cases. About 51% and 39.5% of the pixels show both redshifts (areas (1) and (2)) or both blueshifts (areas (5) and (6)), respectively. The results from the simulations follow a distribution similar to the observational results (Figure 4(b)), although not covering the full observed range, especially with a marked lack of pronounced blueshifts. The models with a cutoff energy of 10 keV and 15 keV match well the high density function regions (nearby 0 km $s^{-1}$ for both lines) from the observations. The models related to thermal conduction (C1, C1+, H1, and H2) or a low cutoff energy (E1 and E1+) show relatively strong redshifts.

It is noteworthy that most of the observational data are located above the $y = x$ line. It means that the centroid velocity of the Mg II k line is usually greater than that of Mg II h line. To interpret this phenomenon, we consider the upward and downward cases separately. In the downward motion case (areas (1) and (2)), for which the energy is conducted from above, considering the direction of progress and formation heights of the two lines, the k and h Doppler velocities correspond to the velocity before and after passage of the perturbation through the specific chromospheric layer, respectively. Thus, the fact that most downward pixels show a faster k velocity than h velocity (area (2)) implies deceleration. This seems reasonable because the material moves to a denser lower region. Similarly, the upward motion case also shows deceleration (area (5)). This may be due to the effects of gravity (ballistic motion) or a loss of kinetic energy.

Interestingly, the correlation between the Mg II h3 and k3 Doppler velocities shows very similar features (Figure 4(c)). Their Pearson correlation coefficient is 0.98, which is almost the same compared with the coefficient obtained by using the centroid velocities. The h3 and k3 Doppler velocities have the same signs of the h and k centroids, and similarly suggest deceleration in both the upward and downward cases. However, we note that the Mg II h centroid is not strongly correlated with the Mg II h3 velocity (Figure 4(d)), and the same holds true for the Mg II k line. We investigated the shapes of the Mg II profiles and found that Mg II h3 positions are occasionally shifted from the centroid of the h line, i.e., the Mg II h spectral line is not symmetric. If the Mg II h3 Doppler velocity and centroid velocity represent motion in the upper chromosphere and averaged chromosphere, respectively, their weak correlation indicates that the upper choromospheric motions are different from the averaged chromospheric motions, and very complex dynamics characterize the chromosphere when nanoflares occur.

#### 3.2.3. Si IV Nonthermal Velocity and $\mu = \cos\theta$

The origin of the nonthermal broadening of spectral lines is a long-standing unsolved mystery. One possibility is that it is caused by unresolved motions. The relation between nonthermal broadening and the magnetic field direction can provide constraints on the possible mechanisms driving these unresolved motions. In particular, Alfvén waves are expected to cause motions perpendicular to the magnetic field direction. We investigated moss regions in active regions, i.e., the foot points of hot coronal loops, so we can hypothesize that the magnetic field direction is very likely perpendicular to the solar surface. In our sample we have moss data at various positions on the solar disk with different $\mu = \cos\theta$. Thus, by analysing the relation between their location from the solar disk center and nonthermal velocity, we can obtain some information about the physical origin of the observed nonthermal broadening.

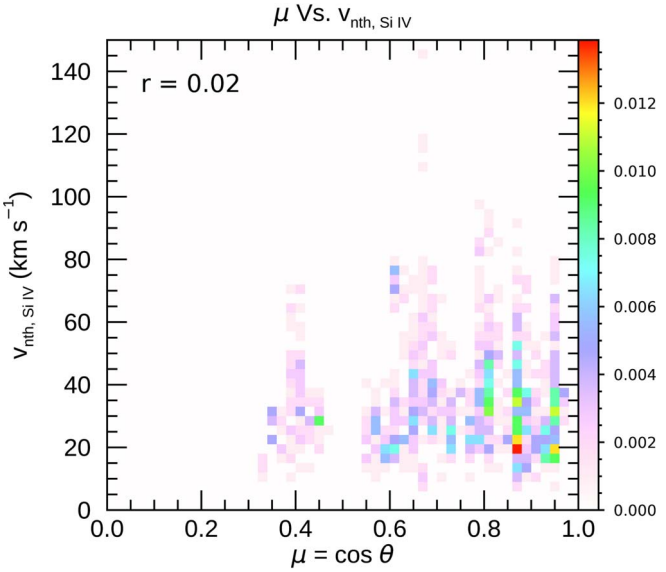


**Figure 5.** The joint probability density function between $\mu = \cos\theta$ and the Si IV nonthermal velocity. The format is the same as in Figure 3.

Our results, shown in Figure 5, demonstrate that the measured nonthermal broadening does not appear to have any clear dependence on the distance from the solar disk center. Most of the Si IV nonthermal velocities show values between 15 and 40 km $s^{-1}$ regardless of the $\mu$ values. The Pearson correlation coefficient is 0.02, which means that the two parameters do not have a linear correlation. These findings suggest that nonthermal broadening is not related to the direction of magnetic fields, hinting that Alfvén waves do not provide a significant contribution to the heating in these events.

#### 3.2.4. Mg II Triplet Emission

The Mg II triplet equivalent width is correlated with the total intensity and the Gaussian amplitude of the Si IV line (Figures 6(a) and (b)). Those two parameters of Si IV have a strong correlation with each other (in Section 3.2.1), therefore it is not surprising that if a correlation with the Mg II triplet equivalent width is found, it will be found for both parameters with similar correlation coefficients. According to theoretical calculations and numerical simulations, the Mg II triplet is formed in the low chromosphere, and it is in emission in the presence of a steep temperature increase in the lower chromosphere (Pereira et al. 2015), while Si IV is formed in the lower transition region (e.g., Dudík et al. 2014). The RADYN simulations also predict a weak correlation between the Mg II triplet equivalent width and line intensity as observed; nonthermal electrons of sufficient energy will penetrate deeper in the atmosphere and deposit their energy in the chromosphere simultaneously causing Mg II triplet emission and strong Si IV emission, while heating in the corona and subsequent conduction (or nonthermal electron with low energies $\lesssim$5 keV) produces weaker Si IV emission, no significant heating in

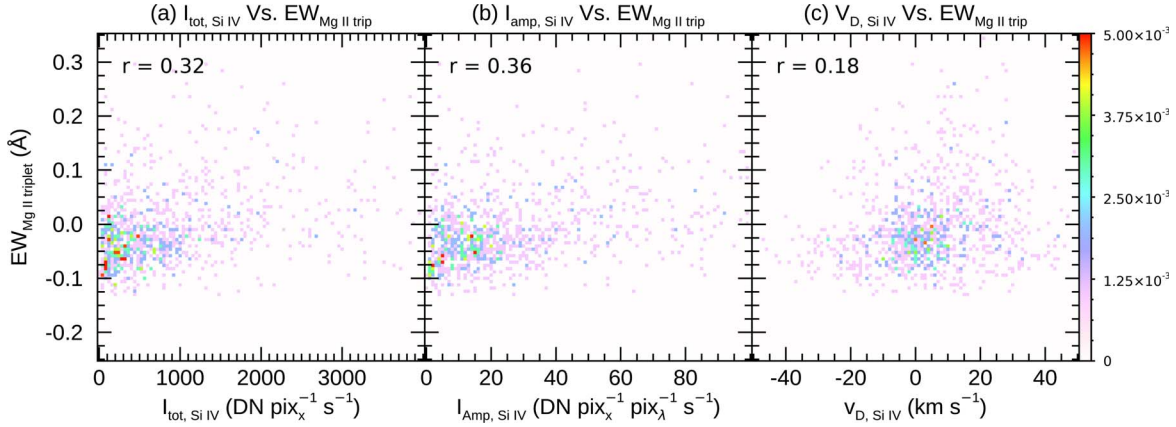


**Figure 6.** Joint probability density function between the equivalent width of the Mg II triplet and Si IV parameters: (a) total intensity, (b) Gaussian amplitude, and (c) Doppler velocity. The format is the same as in Figure 3.

the lower chromosphere, and therefore a negative Mg II equivalent width. However, from the models we would also expect a negative correlation of the Mg II triplet emission with the Si IV Doppler shift, which is not evident in the observations (Figure 6(c)).

#### 3.2.5. *Fe XVIII Intensity*

Fe XVIII emission is a representative parameter reflecting the amount of coronal plasma hotter than ∼4 MK, which clearly correlates with the activity level of the active region, as can be deduced from Figure 2(b). However, the Fe XVIII emission value we derive is spatially averaged (in the IRIS FOV; see Section 2), at the time of moss brightening and therefore can provide some information on the possible effect of the instantaneous coronal environment on the properties of the heating.

We find that the Fe XVIII emission shows some correlation, although weak, with the total intensity of Si IV and with the equivalent width of the Mg II triplet (Figure 7). As discussed in the previous section, our RADYN simulations suggest that these two parameters have some dependence on the parameters of the heating, and in particular that they are enhanced when accelerated electrons of sufficiently high energy (i.e., a low-energy cutoff $\gtrsim$10 keV) are present, because these nonthermal particles efficiently heat the lower atmosphere. Therefore, we can speculate that active regions producing more hot plasma might more easily accelerate electrons to high energies.

## 4. Conclusion and Discussion

The transition region response to coronal heating events provides very powerful diagnostics of the heating properties. Here we have carried out a statistical study of IRIS spectral observations of moss brightenings caused by small-scale heating events (nanoflares). We have further developed an algorithm to detect moss brightenings automatically from SDO/AIA and IRIS data (Graham et al. 2019). We have found more than 1000 moss brightenings, and analysed the IRIS Si IV and Mg II emission, extracting their spectral parameters, and analysing their distributions and the relations among the different parameters.

The automatic detection algorithm allowed us to detect a broader range of events, compared with the manually selected sample we analysed in previous work (Testa et al. 2014, 2020). Overall, we find that the parameters derived from our much large sample of events are mostly in agreement with the previous smaller studies. In particular, we note that the Si IV Doppler velocity has a similar, roughly symmetric, distribution between approximately −40 and 40 km $s^{-1}$, and that Mg II triplet emission (here identified by positive values of the equivalent width of the line) is found for a non-negligible fraction of the sample ($\gtrsim$30%). Some observed properties also show some differences. For instance the nonthermal broadening distribution of our sample covers a much broader range of values than in the previous works. We note that in Testa et al. (2020), rather than analysing the absolute values of nonthermal broadening, we had derived the relative increases compared to the quiescent spectra outside of the brightenings. By taking that into account, the values found in the smaller sample of Testa et al. (2020) would correspond to a range of roughly 15–60 km $s^{-1}$, not too dissimilar to the bulk of our distribution, although their distribution peaked at the lower end, while we find a mean value of ∼32 km $s^{-1}$. Also, we detected a large number of weaker events, as indicated by the histograms showing the distributions of the Si IV total intensity (Figure 2(e)) and amplitude (Figure 2(f)). Testa et al. (2020, 2014) reported about a dozen transient moss brightenings. For several of their events the maximum amplitude of the Si IV was $\gtrsim$40 DN $pix_x^{-1}$ $pix_\lambda^{-1}$ $s^{-1}$, slightly larger than our results with a mean value of about 30 DN $pix_x^{-1}$ $pix_\lambda^{-1}$ $s^{-1}$. This preference for weaker events from the automatic detection algorithm is presumably due to the fact that smaller events occur more frequently. It may indicate that the brightenings we found are scaled-down version of large flares, and their occurrence rate perhaps follow a power law (e.g., Aschwanden et al. 2000). We briefly tested that the Si IV total intensity roughly follows a power-law distribution with a power of −0.71; however, further studies are required to obtain the total energy of nanoflares from Si IV spectral data.

We examined the dependence of the moss brightenings on the coronal environment. In Figure 2(b), the flare productive active regions show relatively higher Fe XVIII intensities, which indicate the existence of a larger amount of hot plasma in the corona. The Fe XVIII emission shows a moderate positive correlation with the total intensity of the Si IV line, and with the equivalent width of the Mg II triplet line (Figure 7), which can be used as a rough indicator of the cutoff energy of the electron beam, according to the numerical simulations (Figure 2(k); Testa et al. 2020). In addition, we found that the moss brightenings occurred more frequently in flare productive

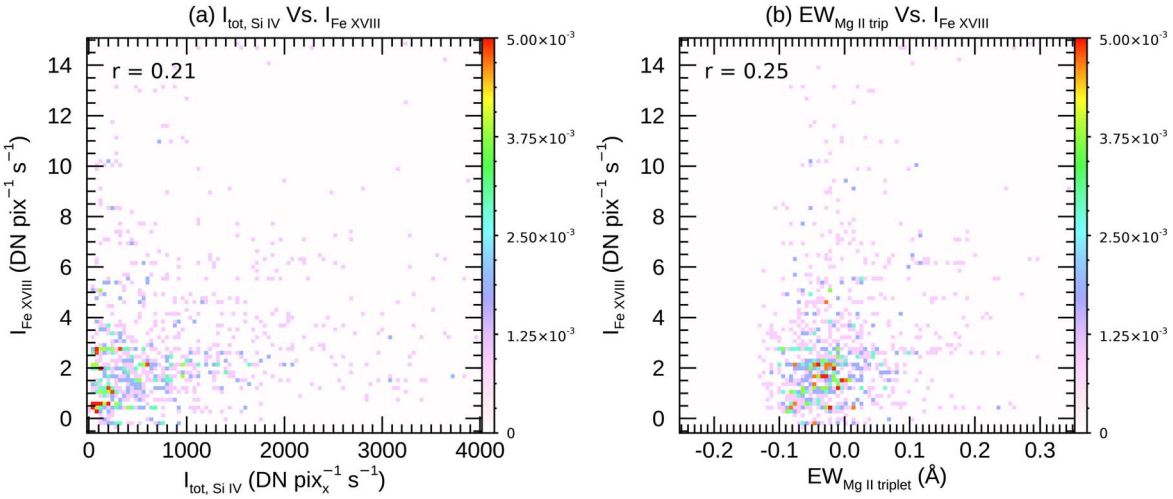


**Figure 7.** Joint probability density function between the Fe XVIII intensity and (a) Si IV total intensity and (b) equivalent width of the Mg II triplet. The format is the same as in Figure 3.

active regions. Thus, we conjecture that in vigorous active regions with hot plasma, higher energy electron beams can be generated more frequently.

As noted above, compared with our previous work based on small samples of these heating events, here we derived more parameters, and the size of our sample allowed for a statistical analysis of the relations between the parameters. For the Si IV line (Figure 3), we found that the total intensity is well correlated with the Gaussian amplitude of the line, as expected. In our sample we found no significant correlation between the nonthermal velocity and Si IV Gaussian amplitude, in contrast with the results of previous work on an entire active region (De Pontieu et al. 2015). As we discussed above (Section 3.2.1), this might be explained by the significant presence of multiple emission components or because the atmospheric structure disturbed by accelerated particles differs from that of typical active regions. Another very interesting correlation we found is between the chromospheric (Mg II h&k) and transition region Doppler velocities, which show a significant positive correlation (Figure 4). This finding points to the fact that heating events might impact different layers of the atmosphere similarly. In particular, the Mg II h and k lines have a very strong correlation of velocities, either measured by the line centroids or the positions of the h3/k3 lines. In both cases the velocity of the k line (formed at slightly larger heights than h) is slightly larger than for the h line, for both redshifted and blueshifted cases, suggesting a deceleration in both cases. However, it is interesting to note that the velocities from the Mg II centroid or the h3/k3 positions only show a modest correlation ($r = 0.27$), indicating that the Mg II h&k lines are mostly asymmetric, and, in turn, this suggests that these heating events are characterized by strong flows and gradients in the chromosphere.

To investigate the nature of the nonthermal velocity, we analysed its relation with the distance from the solar disk center, i.e., with inclination with respect to the line of sight. We found that the nonthermal velocity does not have a significant correlation with the distance from the solar disk center (Figure 5). Previous studies reported that center-to-limb variations of nonthermal velocities or line widths are negligible (e.g., Chae et al. 1998; Ghosh et al. 2021). Our work confirms this lack of correlation is also valid in moss brightening regions. This could occur because the turbulent motions are isotropic, or there may be different processes that act along the field and perpendicular to the field and that are of equal magnitude (De Pontieu et al. 2014; Tian et al. 2014; De Pontieu et al. 2015).

Another finding about the Si IV nonthermal velocity is that the observed values are higher than found in the numerical simulations, and than previous reports. The median value of our measurements is 32 km s$^{-1}$, and the distribution has a long tail to values that are higher than 60 km s$^{-1}$. In contrast, the simulation results show values less than 25 km s$^{-1}$ (Figure 2(g)). This may be attributed to the fact that the simulations do not contain turbulent motions and assumed a single loop, while several thin adjacent magnetic strands, heated around the same time, are likely observed within a single IRIS pixel. Clearly such superposition within one pixel can lead to an increase in nonthermal broadening, given the different velocities along independently heated loops. In De Pontieu et al. (2015), they measured the nonthermal velocities of the Si IV line in an active region, and reported that their distribution is close to a normal distribution with a peak value of about 18 km s$^{-1}$. Our selected events are for moss regions, heated impulsively by conduction or accelerated electron beams, which might contribute to the high nonthermal broadening tail observed in active regions (De Pontieu et al. 2015; Testa et al. 2016). In some of the Si IV spectra in our sample, the very high nonthermal velocities are due to the presence of multiple components.

Thus, it is clear that moss brightenings are usually characterized by violent dynamics. This is evidenced not only by the nonthermal velocity of the Si IV line, but also by the asymmetric profiles of the Mg II spectral lines. An asymmetric profile implies that the h3 or k3 position is shifted with respect to the line centroid, so the upper chromospheric motion is not consistent with the average chromospheric motion. Moreover, the difference of h2v and h2r intensities indicates strong upward or downward motion (Carlsson & Stein 1997b; Leenaarts et al. 2013).

By comparison with the numerical simulations, our results help to understand the nanoflare mechanism and provide constraint on the physical parameters. Our numerical simulations with various model parameters reproduce fairly well the

Si IV and Mg II spectral properties when nanoflares occur. Most of the parameters have similar values to the observations. In agreement with our previous work (Testa et al. 2014; Polito et al. 2018; Testa et al. 2020), the observed Si IV blueshifted profiles, as well as the Mg II triplet emission, are only reproduced by simulations including heating by beams of accelerated electrons. However, several parameters deviate from the observational data, pointing to interesting issues that need to be investigated in more detail, and to the need for additional models that can more consistently explain the observations. Some examples include the relatively small nonthermal velocity, and the lack of a significantly large negative value of the Mg II centroid velocities in the simulations (Figures 2(g), (i), and (j)). As we speculated earlier in the paper, the former might be due to the fact that the single loop models might not be an adequate comparison for the observations in each IRIS pixel where many strands, possibly with significantly different initial conditions and heating properties, might overlap. The latter might be due to shortcomings of the model in reproducing realistic chromospheric conditions as discussed at length in previous literature (e.g., see the discussion in Polito et al. 2018). Another puzzling discrepancy between simulations and observations is the relation between the Si IV Doppler velocity and the equivalent width of the Mg II triplet. The numerical simulations characterized by blueshifts also have stronger Mg II triplet emission, whereas the two parameters appear to have a very weak but positive correlation in the observational data (Figure 6(c)). It is possible that our definition of the equivalent width does not adequately capture Mg II emission in the observations, but this discrepancy will be thoroughly investigated in future work.

In summary this work has presented a thorough analysis of the observational signatures of the lower atmospheric (chromosphere and transition region) response to small coronal heating events. The comparison with RADYN simulations of nanoflare-heated loops has highlighted the overall agreement between the predictions and the observations for individual, single observables (e.g., intensity). However, we have also found some discrepancies, and there are no specific models that explain all the observed parameters simultaneously. These limitations shed light on the shortcoming of the models and emphasize the need for more diverse and realistic numerical simulations to yield a more comprehensive reproduction of the observed signatures and interpretation of the data.

We gratefully acknowledge support by the NASA contract NNG09FA40C (IRIS). This research has made use of NASA's Astrophysics Data System and of the SolarSoft package for IDL. IRIS is a NASA small explorer mission developed and operated by LMSAL with mission operations executed at NASA Ames Research Center and major contributions to downlink communications funded by ESA and the Norwegian Space Centre. Resources supporting this work were provided by the NASA High-End Computing (HEC) Program through the NASA Advanced Supercomputing (NAS) Division at Ames Research Center. CHIANTI is a collaborative project involving George Mason University, the University of Michigan (USA), University of Cambridge (UK) and NASA Goddard Space Flight Center (USA).

## Appendix
## Joint Probability Density Functions for all Parameters

Figure A1 shows joint probability density functions for all eleven parameters. In most cases, the Pearson correlation coefficients are very small ($|r| < 0.2$). We chose some significant relationships and explained in Section 3.2.

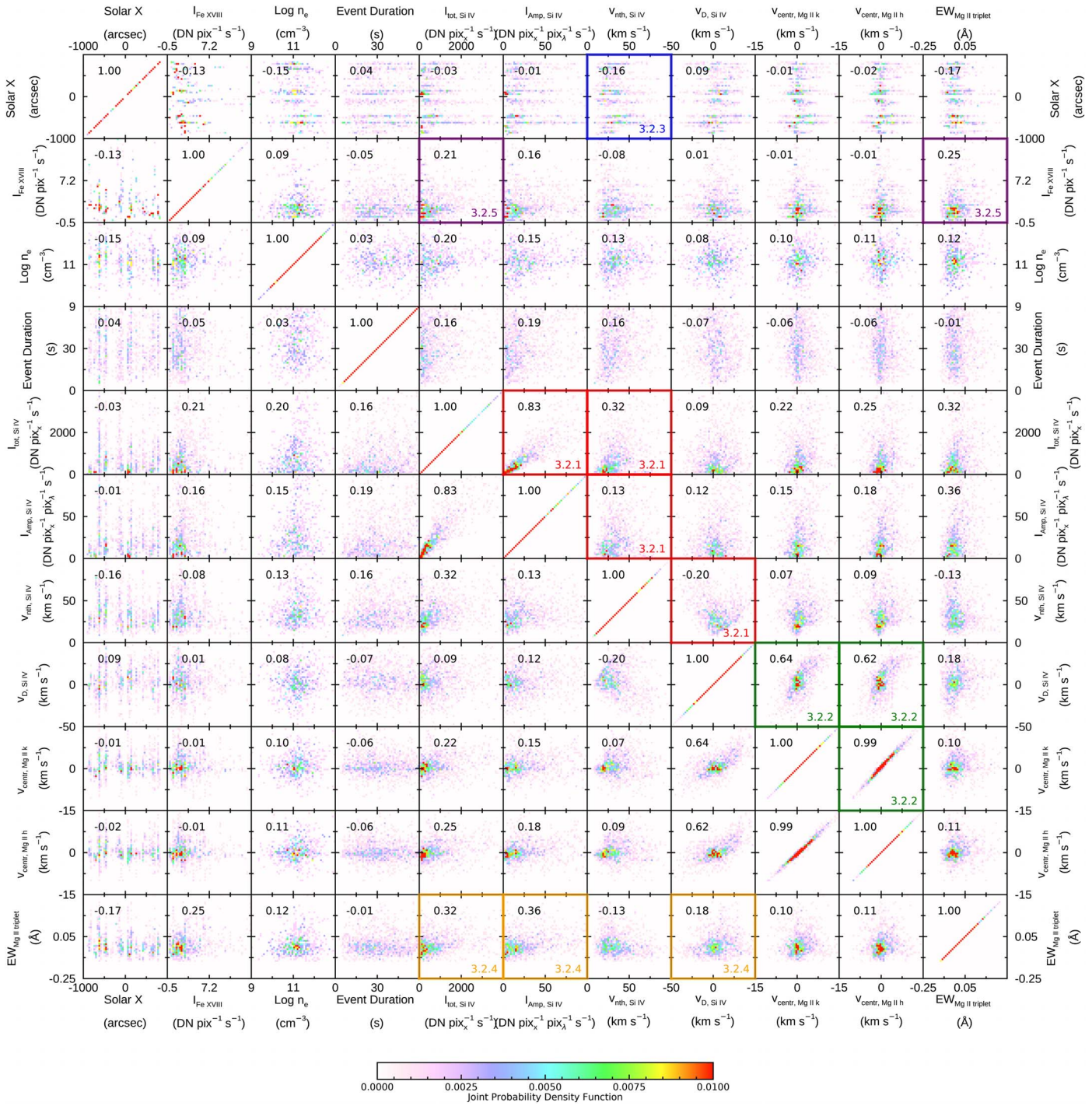


**Figure A1.** Joint probability density functions for all parameters. The image is diagonally symmetric, but we show the entire matrix of combinations for the reader's convenience. The Pearson correlation coefficient between two parameters is shown in the top left corner of each plot. The colored boxes with red, green, blue, orange, and purple are related to Sections 3.2.1–3.2.5, respectively.

## ORCID iDs

Kyuhyoun Cho https://orcid.org/0000-0001-7460-725X
Paola Testa https://orcid.org/0000-0002-0405-0668
Bart De Pontieu https://orcid.org/0000-0002-8370-952X
Vanessa Polito https://orcid.org/0000-0002-4980-7126

## References

Allred, J. C., Kowalski, A. F., & Carlsson, M. 2015, ApJ, 809, 104
Antiochos, S. K., Karpen, J. T., DeLuca, E. E., Golub, L., & Hamilton, P. 2003, ApJ, 590, 547
Aschwanden, M. J., Tarbell, T. D., Nightingale, R. W., et al. 2000, ApJ, 535, 1047
Bakke, H., Carlsson, M., Rouppe van der Voort, L., et al. 2022, A&A, 659, A186
Carlsson, M., & Stein, R. F. 1992, ApJL, 397, L59
Carlsson, M., & Stein, R. F. 1995, ApJL, 440, L29
Carlsson, M., & Stein, R. F. 1997a, in Solar and Heliospheric Plasma Physics. Lecture Notes in Physics, ed. G. M., Simnett, C. E. Alissandrakis, & L. Vlahos, Vol. 489 (Berlin: Springer), 159
Carlsson, M., & Stein, R. F. 1997b, ApJ, 481, 500
Chae, J., Schühle, U., & Lemaire, P. 1998, ApJ, 505, 957
Cheung, M. C. M., Boerner, P., Schrijver, C. J., et al. 2015, ApJ, 807, 143
Cooper, K., Hannah, I. G., Grefenstette, B. W., et al. 2021, MNRAS, 507, 3936
Curdt, W., Landi, E., & Feldman, U. 2004, A&A, 427, 1045
De Pontieu, B., Berger, T. E., Schrijver, C. J., & Title, A. M. 1999, SoPh, 190, 419
De Pontieu, B., McIntosh, S., Martinez-Sykora, J., Peter, H., & Pereira, T. M. D. 2015, ApJL, 799, L12
De Pontieu, B., Rouppe van der Voort, L., McIntosh, S. W., et al. 2014, Sci, 346, 1255732
De Pontieu, B., Title, A. M., Lemen, J. R., et al. 2014, SoPh, 289, 2733
Del Zanna, G. 2013, A&A, 558, A73
Dudík, J., Del Zanna, G., Dzifčáková, E., Mason, H. E., & Golub, L. 2014, ApJL, 780, L12
Ghosh, A., Tripathi, D., & Klimchuk, J. A. 2021, ApJ, 913, 151
Glesener, L., Krucker, S., Duncan, J., et al. 2020, ApJL, 891, L34
Graham, D. R., De Pontieu, B., & Testa, P. 2019, ApJL, 880, L12
Hale, G. E., Ellerman, F., Nicholson, S. B., & Joy, A. H. 1919, ApJ, 49, 153
Hannah, I. G., Christe, S., Krucker, S., et al. 2008, ApJ, 677, 704
Holman, G. D., Aschwanden, M. J., Aurass, H., et al. 2011, SSRv, 159, 107
Klimchuk, J. A. 2006, SoPh, 234, 41
Künzel, H. 1965, AN, 288, 177
Leenaarts, J., Pereira, T. M. D., Carlsson, M., Uitenbroek, H., & De Pontieu, B. 2013, ApJ, 772, 90
Lemen, J. R., Title, A. M., Akin, D. J., et al. 2012, SoPh, 275, 17
Parker, E. N. 1988, ApJ, 330, 474
Pereira, T. M. D., Carlsson, M., Pontieu, B. D., & Hansteen, V. 2015, ApJ, 806, 14
Pereira, T. M. D., & Uitenbroek, H. 2015, A&A, 574, A3
Pesnell, W. D., Thompson, B. J., & Chamberlin, P. C. 2012, SoPh, 275, 3
Polito, V., Testa, P., Allred, J., et al. 2018, ApJ, 856, 178
Schmit, D., Bryans, P., Pontieu, B. D., et al. 2015, ApJ, 811, 127
Testa, P., De Pontieu, B., Allred, J., et al. 2014, Sci, 346, 1255724
Testa, P., De Pontieu, B., Martínez-Sykora, J., et al. 2013, ApJL, 770, L1
Testa, P., Polito, V., & Pontieu, B. D. 2020, ApJ, 889, 124
Testa, P., Pontieu, B. D., & Hansteen, V. 2016, ApJ, 827, 99
Testa, P., & Reale, F. 2012, ApJL, 750, L10
Testa, P., & Reale, F. 2022, arXiv:2206.03530
Testa, P., Saar, S. H., & Drake, J. J. 2015, RSPTA, 373, 20140259
Tian, H., DeLuca, E. E., Cranmer, S. R., et al. 2014, Sci, 346, 1255711
Toriumi, S., & Wang, H. 2019, LRSP, 16, 3
Uitenbroek, H. 2001, ApJ, 557, 389
Wright, P. J., Hannah, I. G., Grefenstette, B. W., et al. 2017, ApJ, 844, 132